Chapter

Simple Preparations for Plasmon-Enhanced Photodetectors

Yu Liu, Junxiong Guo, Jianfeng Jiang, Wenjie Chen, Linyuan Zhao, Weijun Chen, Renrong Liang and Jun Xu

Abstract

Localized surface plasmon resonance (LSPR), known as the collective oscillation of electrons and incident light in metallic nanostructures, has been applied in high performance photodetectors over the past few years. But the preparation process is complex and expensive due to the introduction of electron beam lithography (EBL) for preparing nanostructures. In the past few months, we have demonstrated two simple methods to prepare plasmon-enhanced photodetectors: (i) Au nanoparticles (Au NPs) solution were directly spun coated onto the WS_2-based photodetectors. The performance has been enhanced by the LSPR of Au NPs, and reached an excellent high responsivity of 1050 A/W at the wavelength of 590 nm. (ii) Au NPs were deposited on MoS_2 by magnetron sputtering. The spectral response of pure MoS_2 was located in visible light and which was extended to near-infrared region (700–1600 nm) by Au NPs. Further, the responsivity reaches up to 64 mA/W when the incident light is 980 nm. In this book chapter, more details for developing those two simple methods and the discussion of the enhanced mechanism are performed, which can be very useful for the next generation photodetection.

Keywords: surface plasmon resonance, Au nanoparticles, enhanced photodetectors, simple preparations, high responsivity

1. Introduction

Photodetectors are one of the most important devices in photonic chips, which show a great potential in optical communication, flame sensing, environmental monitoring, and astronomical studies [1]. A lot of semiconductors have been exploited for photodetection such as silicon, GaN, PbS, InGaAs and HgCdTe, operating from ultraviolet to far-infrared region [2]. It is significant to decrease the dimension of photodetectors down to the sub-nano scale for the next generation highly integrated photonic chips.

Two-dimensional (2D) materials such as graphene and layered transition metal dichalcogenides (TMDs) have attractive electronic and optical properties such as flexibility, transparency and metal-oxide-semiconductor (CMOS) compatibility [3–7]. Tungsten disulfide (WS_2), a typical member of the TMDs group, has a higher carrier mobility than other TMD materials due to smaller electron effective mass [8]. Moreover, WS_2 enjoys excellent thermal stability for extensive applications [9].

Hence, WS_2-based high stable photodetectors can be used in many attractive applications such as extreme environment detection. Furthermore, Two-dimensional stacked molybdenum disulfide (MoS_2) has attracted many research interests for applications in optoelectronic devices, due to its outstanding merits of electronic and optical properties, especially photodetectors. But the few layers 2D material-based photodetectors suffer from low photoresponsivity mainly due to the poor optical absorption in the atomic layered materials.

A number of 2D material-based photodetectors have been enhanced using resonance microcavity, PbS quantum dots, tunneling effect, heterojunctions or perovskite [10–14]. The narrow band absorption or complex preparation process limits the application of these attractive methods. Recently, localized surface plasmon resonance (LSPR)-enhanced photodetector has been demonstrated, and we have also provided effective ways to enhance the efficiency of light-harvesting [15–17]. LSPR can be excited by Ag or Au nanoparticles (NPs) such as deep metallic grating, nanodisk array, bowtie array, hybrid antenna and fractal metasurface [18–20]. Furthermore, patterning 2D materials into periodic structure can also excite plasmon resonance [21]. The methods for preparing the nanostructure involve electron beam lithography, hydrothermal synthesis, and template-based electrochemical method, which are generally complicated, expensive and may deleterious to the device.

For the current existing problems, we have demonstrated two methods for easy-preparation and high-performance 2D material-based photodetectors [22, 23]. (i) Au NPs solution was directly spun coated onto WS_2-based photodetectors. The performance has been enhanced by the LSPR of Au NPs, and reach quite high responsivity of 1050 A/W at the wavelength of 590 nm. The diameters and distance of Au NPs will affect the resonant wavelength and absorption of the device. (ii) We have demonstrated a MoS_2 plasmonic photodetector by depositing Au NPs on MoS_2 sheet using magnetron sputtering without need of template, which shows a significant improvement of photo-response in near-infrared region. The spectral response of pure MoS_2 was in visible light and which was extended to near-infrared region (700–1600 nm). Furthermore, the responsivity reaches up to 64 mA/W when the incident light is 980 nm. Detailed preparation and discussion of the mechanism are performed in the chapter.

2. The preparation and theoretical mechanism of spun-coated WS_2-based photodetectors

2.1 The preparation process

The WS_2 film was grown on sapphire substrate by chemical vapor deposition (CVD) method and transferred to Si/SiO_2 substrate by wet transfer method. The molecular configurations of WS_2 are shown in **Figure 1a**. Raman spectra (**Figure 1b**), PL spectrum (**Figure 1c**) and atomic force microscopy (AFM) files (**Figure 1d**) reveal monolayer feature of WS_2 film.

The 3D and cross-section view of the photodetector is shown in **Figure 2a, b**, respectively. The light incident normally from the top of the device. The fabrication was carried out by the following steps. First of all, a 200-nm-thick molybdenum (Mo) layer was deposited and patterned on WS_2 layer. Afterwards, the WS_2 was patterned (size: 30 × 100 μm) by photolithography and plasma etching to form active area. Finally, Au NPs solution was spun coating onto the channel and dried in air. Nearly spherical Au NPs can be seen in the low-resolution transmission electron microscopy (TEM) image (**Figure 2c**). The mean diameter of Au

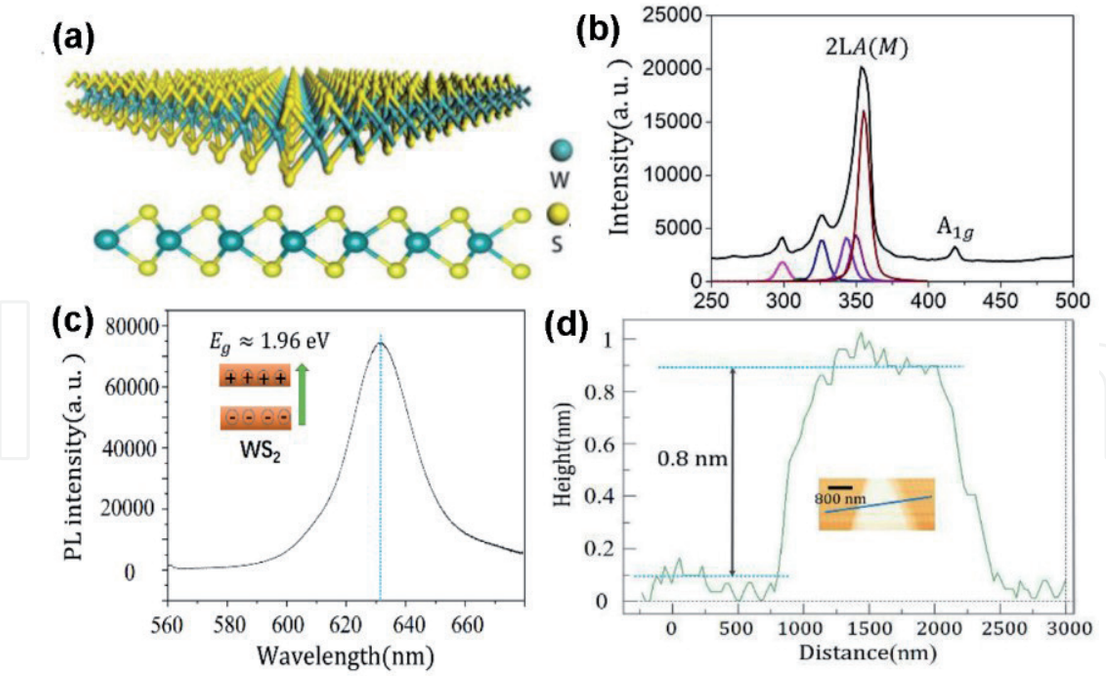

Figure 1.
The microscopic molecular structures and characterization of monolayer WS_2 film [22]. (a) Schematic molecular structure of 1 L-WS_2. The blue and yellow balls present sulfur and tungsten, respectively. (b) The Raman spectrum consisted of several characteristic peaks of the WS_2 film on Si/SiO_2 substrate acquired with laser excitation of λ = 532 nm. (c) PL spectra of 1 L WS_2 layer. The band gap is about 1.96 eV as shown in the inset. (d) The AFM height profiles and corresponding AFM image of 1 L-WS_2. The thickness is about 0.8 nm.

NPs is ~20 nm (**Figure 2d**) as shown in the statistical analysis of the TEM images. Typical low-resolution (**Figure 2e**) and high-resolution (**Figure 2f**) scanning electron microscope (SEM) images of the Au NPs are also presented. The Au NPs are well distributed on the top of the WS_2 film.

2.2 The performance of the WS_2-based photodetector

The drain-source current (I_{DS}) under illumination at room temperature without Au NPs are shown in **Figure 3a**. It is concluded that I_{DS}increase as V_{DS} increase from 0 to 2 V. The irradiance power is 20.5 mW/cm^2 in all of these three wavelength (590, 740 and 850 nm). I_{DS} decrease with the increase of wavelength. The ratio of the on/off current (I_{DS}/I_{dark}) reached nearly 10^3 under 590 nm light illumination. The responsivity can be calculated by

$$R = I_{Ph}/P \tag{1}$$

where I_{Ph} is the photocurrent, P is the irradiance power. The responsivity at V_{DS} = 2 V is illustrated in **Figure 3b**. The responsivity decrease with the increase of the power which are typical for photodetectors [24, 25]. R reached 35 A/W at the wavelength of 590 nm, and reached 1.8 A/W at the wavelength of 850 nm when irradiance power is both 0.2 mW/cm^2. The performance of the photodetector decoated with Au NPs is shown in **Figure 3c**. The drain-source current are measured at the irradiance power of 20.5 mW/cm^2. The enhanced I_{DS} also reached the highest value at 590 nm and decreased with the increase of the wavelength (λ).

The current gain is defined as

$$G = I_{pe}/I_{ph} \tag{2}$$

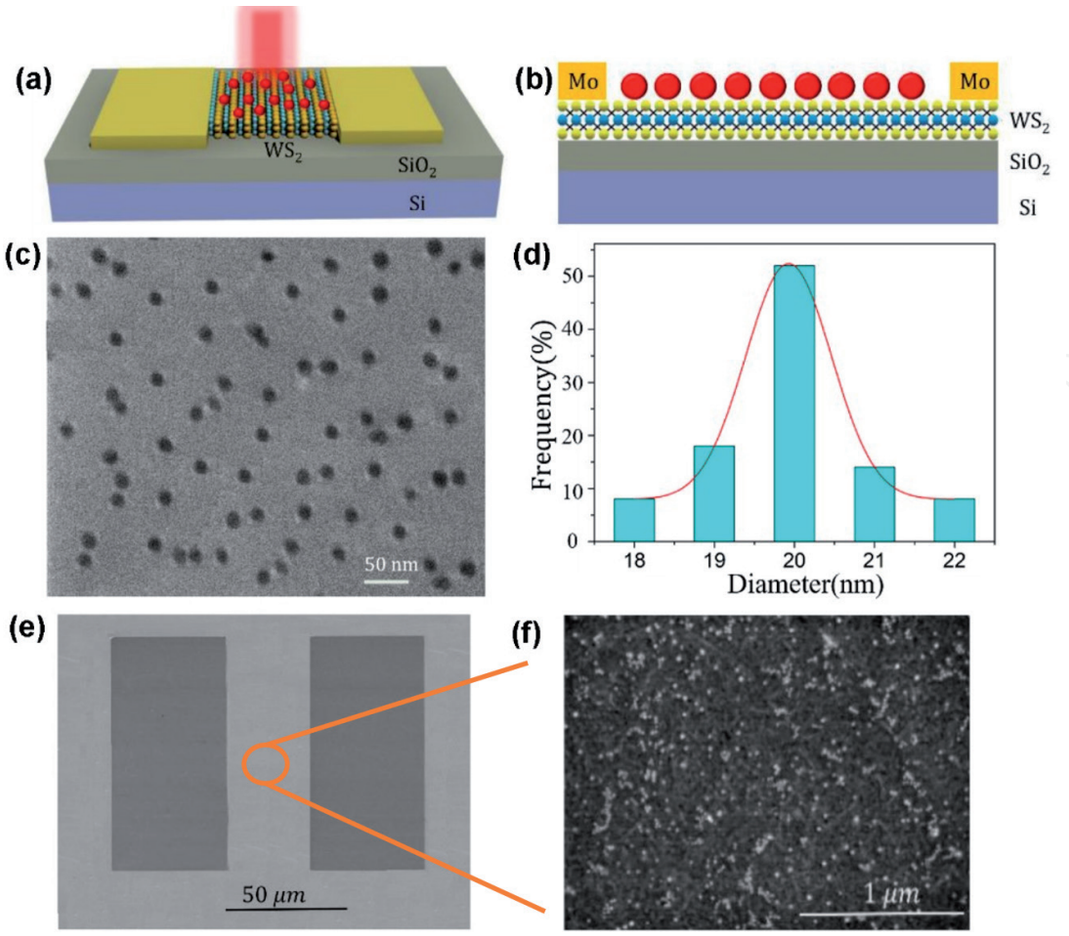

Figure 2.
Characterization of the fabricated photodetector [22]. (a) The schematic 3D view of 1 L-WS_2-based photodetector was presented. The drain/source electrodes are fabricated by Mo. Au NPs (red balls) were spun coated on the channel. (b) The cross-section view of the photodetector. (c) TEM image of Au NPs. The Au NPs are well distributed in the solution. (d) The statistics size distribution of Au NPs based on the TEM image. We can conclude that the mean size of Au NPs is ~20 nm. (e) Low-resolution and (f) high-resolution SEM images of the photodetector. Clear electrodes and An NPs can be seen from these images.

where I_{pe} is the enhanced photocurrent of the photodetector. The current gain reveals the improvement of the device by Au NPs as shown in **Figure 3d** when P =0.2 mW/cm^2 and V_{DS} = 2 *V*. The photoresponsivity was enhanced ~30 times and reached 1050 A/W when λ = 590 nm. The photoresponsivity was enhanced ~11 times and reached 55 A/W when λ = 740 nm. And the photoresponsivity was enhanced ~5 times at near infrared light (λ = 850 nm) and reached 8 A/W. In general, the switching behaviour, which reflect the response speed and high-frequency characteristic, is very important for photodetectors. The detectors also need to quickly refresh in some applications such as instant display. **Figure 3e** presents the switching behavior at near infrared light (λ = 850 nm) of the WS_2 photodetector. The photodetector shows a good repeatability during on-off cycles. Moreover, the on-off characteristic in a period is shown in **Figure 3f**. The rise and decay time are about 100 and 200 ms, respectively.

2.3 The theoretical mechanism

To explain the mechanism of the enhancement by Au NPs, we take finite-difference time-domain (FDTD) method to investigate the distribution of electric field of Au NPs. According to the Förster's expression for energy *W* transferred from donor to acceptor [24, 25].

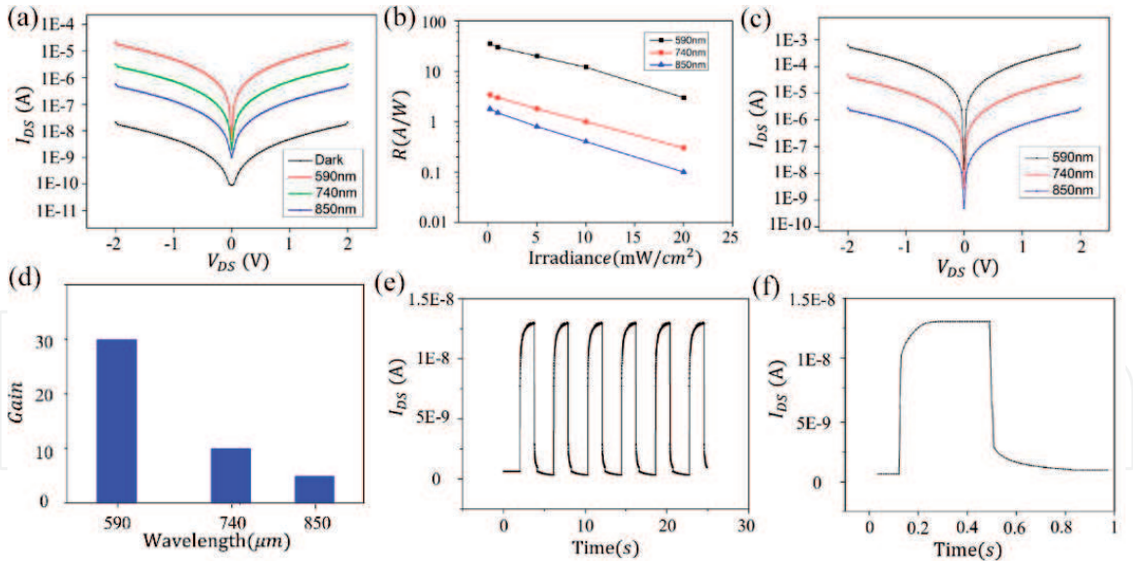

Figure 3.
Visible to NIR light response of the fabricated photodetector [22]. (a) The drain-source current (I_{DS}) changed by the drain-source bias from −2 to 2 V. The optical power is 20.5 mW/cm² for these three wavelength. (b) The photo-responsivity changed as a function of the illumination power when V_{DS} = 2 V. (c) The drain-source current of the photodetector with Au NPs at the same irradiance of 20.5 mW/cm². (d) The current gain of the photodetectors with and without Au NPs when the irradiance is 0.2 mW/cm² and the voltage is 2 V. (e) The on/off behavior of the photodetector when λ = 850 nm. (f) The on-off characteristic of the Au NPs coated photodetector in a period time. The rise time is about 100 ms and the decay time is about 200 ms.

$$\frac{W}{W_d} = \frac{9}{8\pi}\int \frac{d\omega}{k^4} f_d(\omega)\,\sigma_a(\omega)\,|D|^2 \tag{3}$$

where W_d is the donor's energy, $f_d(\omega)$ and k are the spectral function and wave vector of the source, $\sigma_a(\omega)$ is the absorption of acceptor, $D = q/r^3$ is the coupling coefficient, and r is the distance. The performance could be changed by key parameters of Au NPs such as diameter d and distance between two particles s. In order to give an intuitive description, simplified models were built. The distance between the edges of two adjacent nanospheres, s, was fixed on 10 nm. The diameter d was fixed as 20 nm.

The resonant wavelength can be acquired by SPPs dispersion equation.

$$\beta = k_0\sqrt{\frac{\varepsilon_d + \varepsilon_m}{\varepsilon_d \varepsilon_m}} \tag{4}$$

where k_0 is the vacuum wavevector, ε_d is the relative permittivity of dielectric, ε_m is the dielectric function of gold, which can be represented by Drude model. The mismatch of SPPs and incident wavevector can be compensated by the gold nanoparticles, which can be approximately presented by

$$\beta = \sqrt{\varepsilon_d}\,k_0 \sin\theta + \frac{2\pi n}{\lambda_g}\left(\hat{x} + \hat{y}\right) \tag{5}$$

where θ, λ_g, n are the horizontal angle of incident wave vector, the grating period, and an integer, respectively. From Eq. (5), we can see that the absorption wavelength depends only on the dimension of Au NPs.

The results for the illumination at λ =590, 740, and 850 nm are shown in **Figures 4a–c**, respectively. It is clear that the intense electromagnetic fields were introduced by LSPR of Au NPs. The electric field near the Au NPs was significantly enhanced and stronger than the rest region, revealing that electromagnetic energy was compactly confined by the Au NPs. The electromagnetic field was enhanced more significant when the illumination was under λ = 590 nm. The

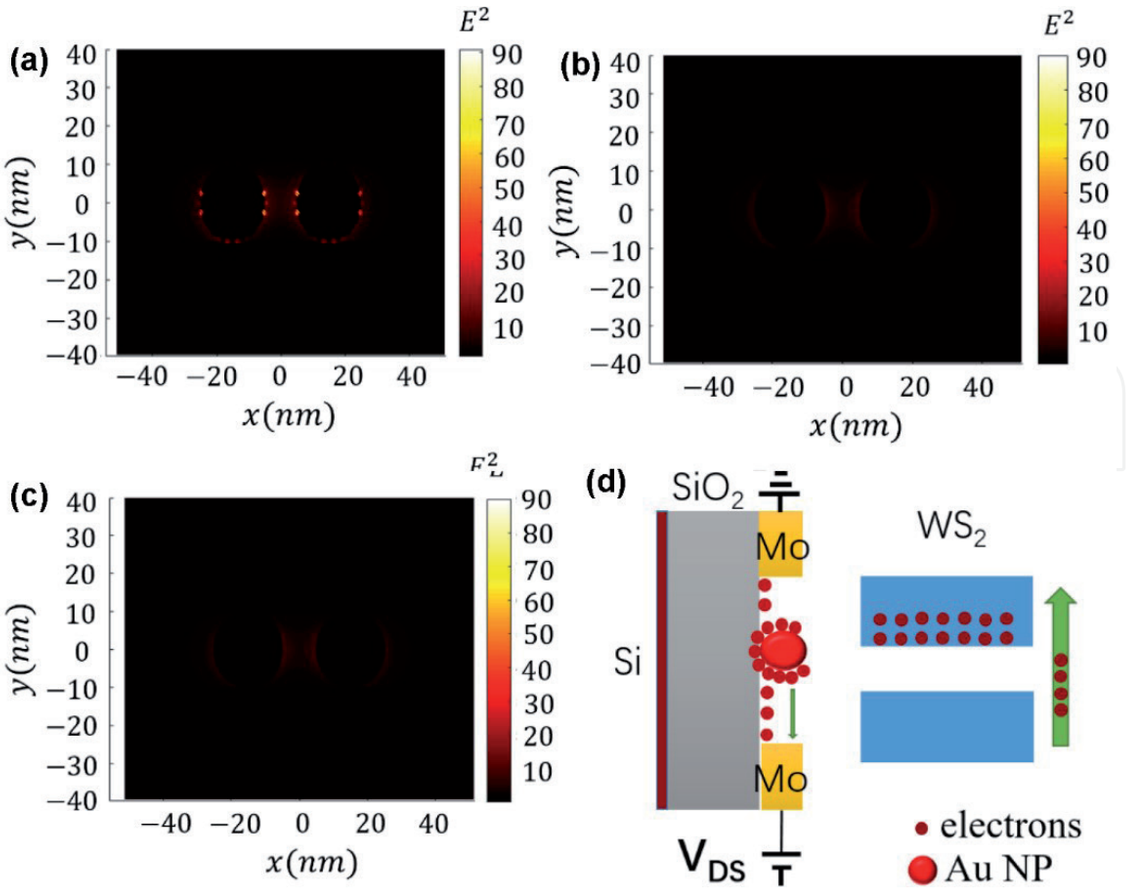

Figure 4.
LSPR and carrier transfer of the presented enhanced photodetector [22]. Cross-section distribution of the square of electric field (|E| 2) near Au NPs under the illumination at the wavelength of (a) 590 nm, (b) 740 nm, and (c) 850 nm. (d) The charge transfer between Au NPs and WS_2 film.

enhanced electric fields could excite the generation of the carriers in the WS_2 film, resulting a prominent photoresponse. The highest responsivity obtained at λ = 590 nm (**Figure 3b, d**) is consistent with the most intense LSPR at λ = 590 nm (**Figure 4a**). The generation and transportation of the electrons are shown in **Figure 4d**. The photons were absorbed by WS_2 film and the excited electrons were driven by the drain-source voltage. There are more electrons around the Au NPs as **Figure 4d** shows.

3. The preparation and theoretical mechanism of magnetron-sputtering-based MoS_2 photodetectors

3.1 The preparation process

Figure 5a, b shows the schematic and optical image of our designed MoS_2 plasmonic photodetector by introducing Au NPs, respectively. The few-layered MoS_2 sheet was obtained using mechanical exfoliation method. Then, we transferred the exfoliated MoS_2 to the SiO_2/Si substrate which contacted with Au/Ni electrodes. Next, we fabricated the Au NPs on exfoliated MoS_2 sheet using magnetron sputtering technique. This facile method offers the convenience of without need of template compared with other reported MoS_2 plasmonic photodetectors.

Figure 6 shows the morphology of as-prepared materials was characterized using an AFM. As shown in Section A1 in **Figure 6a, b**, it indicates the thickness of

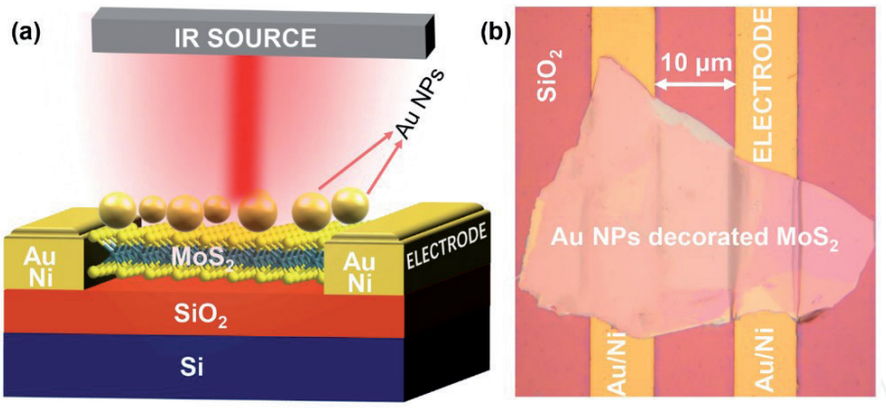

Figure 5.
(a) Schematic and (b) optical image of MoS_2 photodetector decorated with Au NPs [23].

exfoliated bare MoS_2 is just about 6 nm (about 10 folds). In comparison, the surface morphology of the MoS_2 after depositing with Au NPs by magnetron sputtering was shown in **Figure 6c–f**. It clearly exhibits the physical size and particle distribution of Au NPs can be easily tuned by sputtering technique. When the sputtering current increased from 30 mA (LPP1, **Figure 6d**) to 35 mA (HPP1, **Figure 6e**) with deposition period fixed to 1 s, we obtained the controllable Au NPs with lateral size increasing from ~3 to ~5 nm and vertical height increasing from ~5 to ~8 nm, respectively. For another, if we fixed the applied current to 30 mA and prolonged the deposit period to 2 s (LPP2, **Figure 6f**), the Au NPs maintain almost same physical size as LPP1 but the gap of adjacent deposited Au NPs sharply drops compared with LPP1.

3.2 The structure of the MoS_2-based photodetector

In order to investigate chemical composition of the prepared materials, the X-ray photoelectron spectroscopy (XPS) was employed. As shown in **Figure 7**, The peaks at 229.2 and 232.3 eV correspond to the doublet of Mo $3d_{5/2}$ and Mo $3d_{3/2}$, respectively. And the peaks of 226.3, 162.1 and 163.2 eV of the binding energy attach to the S 2s, S $2p_{3/2}$ and S $2p_{1/2}$, respectively [26, 27]. For Au 4f, the peak positions of 83.6 and 87.2 eV bind to the Au $4f_{7/2}$ and Au $4f_{5/f}$, indicating the Au NPs are directly introduced into the exfoliated MoS_2 sheet [28]. More importantly, the banding energies of Mo and S in Au decorated MoS_2 maintain the same values as that of bare MoS_2 sheet, indicating the introduction of Au NPs has non-influence on the crystal structures of exfoliated MoS_2 sheet.

Further, we used Raman spectroscopy of 532 nm laser to confirm the structural properties of the fabricated devices. For MoS_2, the difference of E^1_{2g} and A_{1g}, Δ, corresponding to in-plane and out of plane energy vibrations, is used to index the layer number of obtained MoS_2. **Figure 8a** shows the Δ of bulk MoS_2 and our exfoliated MoS_2 are 27.8 and 25.3 cm^{-1}, respectively, indicating that the thickness of bare MoS_2 is about 10 layers [29], which is highly consistent with the AFM results. After decorating Au NPs with MoS_2, it exhibits the Δ maintains nearly same as bare MoS_2 but the intensities obviously increase, shown in **Figure 8b**, **c**.

3.3 The performance of the MoS_2-based photodetector

The photoelectric performance of the fabricated photodetector was studied at room temperature, which applied a 980 nm laser source with controllable incident power. In order to produce the laser beam pulses, we combined an oscilloscope to

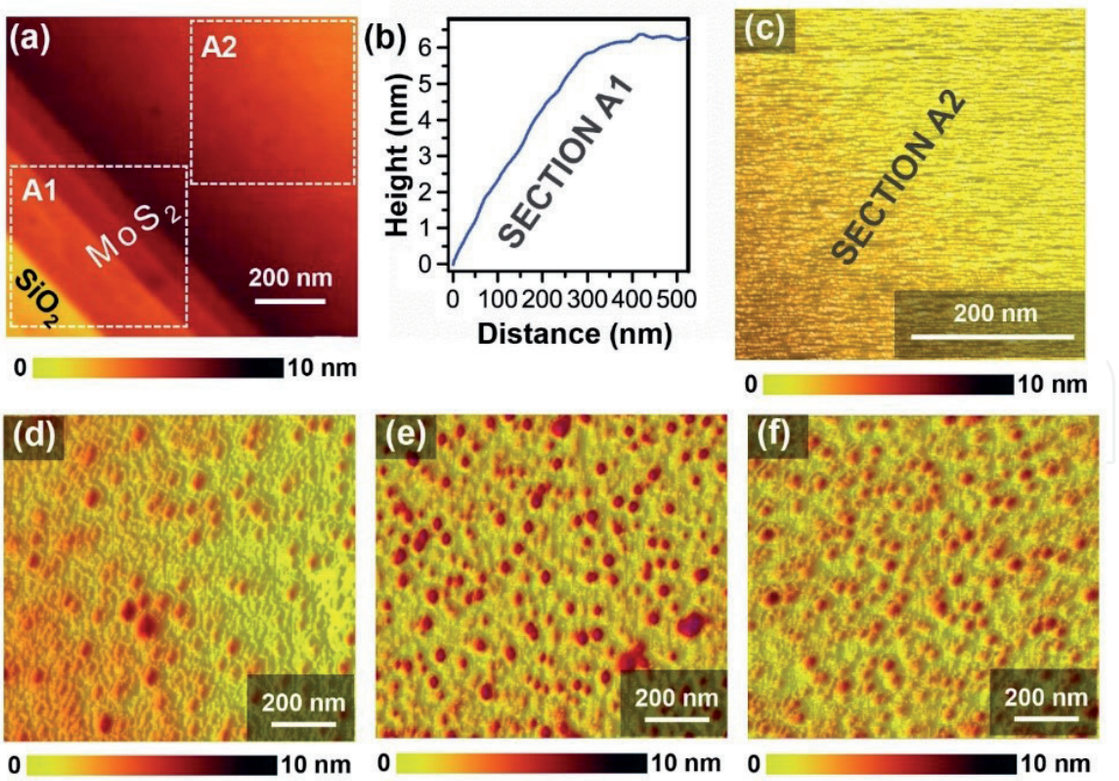

Figure 6.
AFM images of as-prepared bare MoS_2 and MoS_2 modified with Au NPs [23]. (a) Height of exfoliated bare MoS_2 sheet. (b) Height vs. distance plot of bare MoS_2, correspond to the Section A1 in (a). (c) Morphology of bare MoS_2, correspond to the Section A2 in (a). Height of Au NPs decorated MoS_2 sheet for (d) LPP1, (e) HPP1 and (f) LPP2.

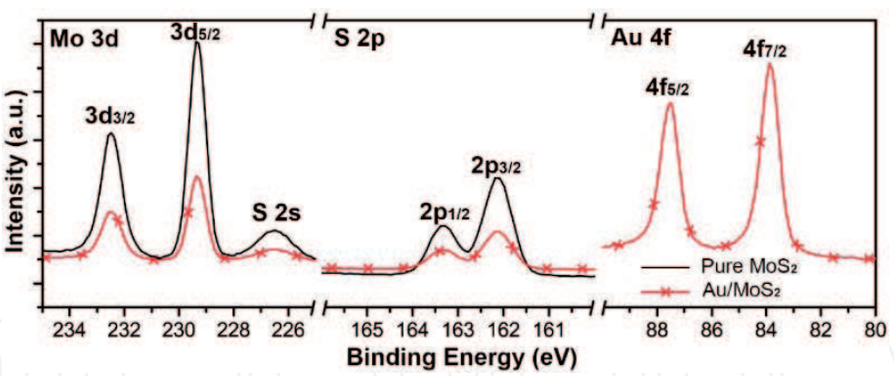

Figure 7.
XPS plots of bare MoS_2 and Au NPs decorated MoS_2 [23].

the incident laser source. **Figure 9a** shows the photocurrent plots of photodetector, where the illumination power and bias voltage are 1.60 mW and 2 V, respectively. Obviously, the Au NPs/MoS_2 heterostructure-based photodetector exhibits an ultra-high photocurrent (8.6 nA) compared with that of bare MoS_2-based photodetector (0.59 nA).

Figure 9b shows the plots of photocurrent vs. applied bias voltage ranging from 0.1 to 15 V. We obtained a photocurrent up to ~480 nA, when the applied incident laser power and bias voltage were 7.50 mW and 15 V, yielding an improved responsibility of 64 mA/W. Moreover, the *I-V* plots indicate the photocurrent owns a good linear relationship with applied bias voltage, when the illumination intensities tuned from 0.85 to 7.5 mW. For another, **Figure 9c** shows the dependence plots of photocurrent (I_{ph}, nA) on laser power irradiation (P_{in}, μW). It is found that the

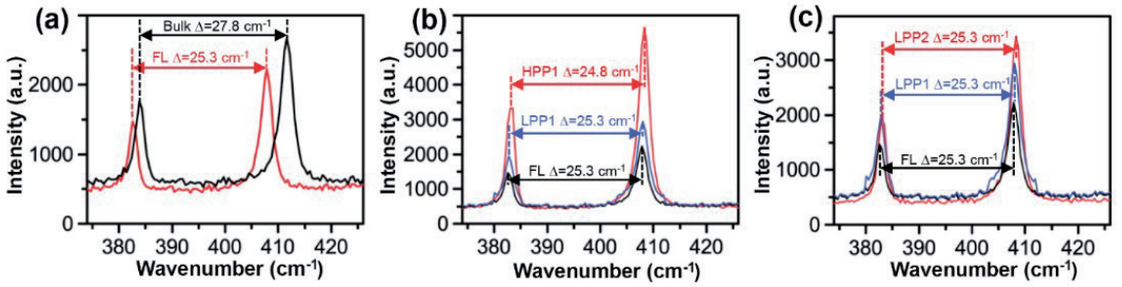

Figure 8.
Raman spectroscopy of the prepared materials. (a) Typical spectra of bulk MoS_2 and exfoliated MoS_2. Raman shift of exfoliated bare MoS_2 sheet and Au NPs decorated MoS_2 with different (b) sputtering electric current (LPP1, HPP1) (c) deposition period (LPP1, LPP2) [23].

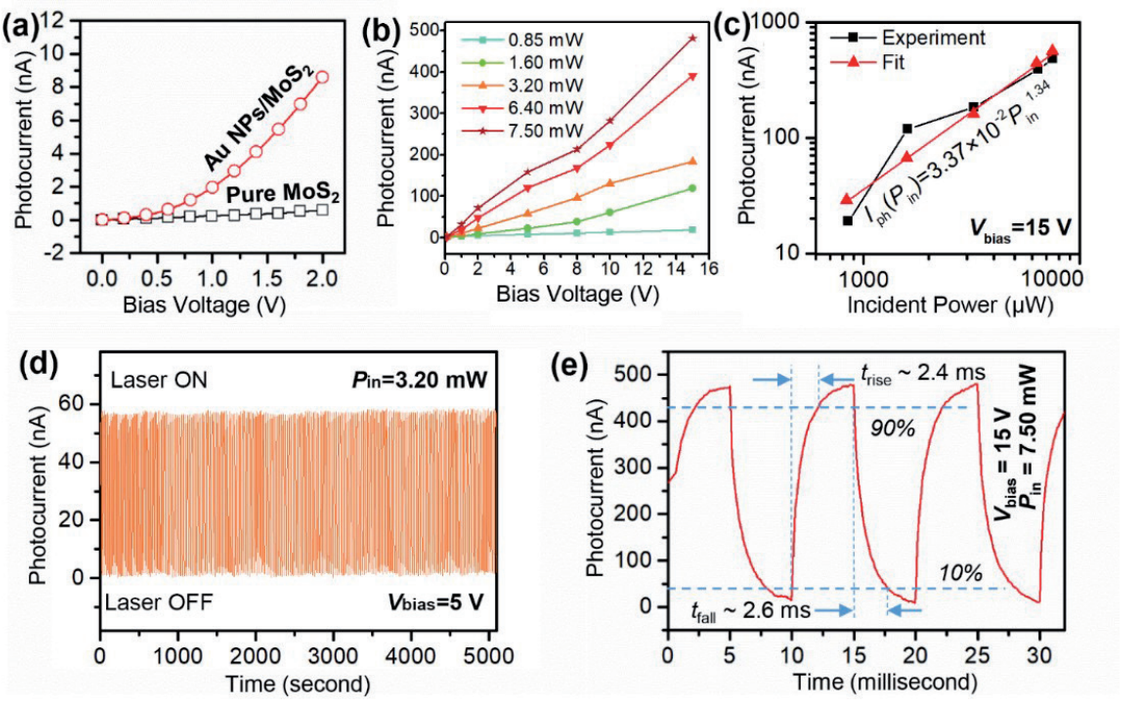

Figure 9.
Photoelectrical performances of Au NPs/MoS_2-based photodetector [23]. (a) I-V plots of photodetectors based on bare MoS_2 and Au NPs decorated MoS_2. (b) I-V scatters of Au NPs/MoS_2-based photodetector with different laser power irradiation ranging from 0.85 to 7.50 mW. (c) Photocurrent as a function of laser power under bias of 15 V. (d) Stability of the fabricated Au NPs/MoS_2-based photodetector. (e) Time response of the fabricated Au NPs/MoS_2-based photodetector.

photocurrent follows a nonlinear dependence to the incident power intensity, $aP_{\text{in}}{}^{b}$, where a and b are constant for different bias voltage. For example, when the bias voltage are 15 V, the fitting a and b are 3.37 × 1o^{-2} and 1.34, respectively.

With respect to the stability of the photodetector, we performed the extended duration photocurrent measurements by periodically switching the incident laser under illumination of 3.20 mW at bias of 5 V, and the periods of both on and off state are 5 s. **Figure 9d** shows the photocurrents over 500 circles of continuous operation, exhibiting a well stability. Moreover, in order to characterize the response time for detecting infrared wavelengths of our designed device, we applied an oscilloscope in the process of laser excitation to produce laser pulses with a duration of 10 ms. **Figure 9e** shows the time-response of Au decorated MoS_2-based device under illumination of 7.50 mW at bias of 15 V. It indicates that the rise time (t_{rise}) and fall time (t_{fall}) are 2.4 and 2.6 ms, respectively, which are significantly superb to that of other reported MoS_2 photodetectors.

3.4 The operational mechanism

In order to study the potential mechanism of our fabricated photodetector, we simulated the electric field distribution of Au decorated MoS_2 using finite element method in the infrared region. We assumed that the Au NPs with a gap of 6 nm and a diameter of 5 nm under illumination of a linearly polarized plane wave with an electric field amplitude of 1 Vm^{-1} for the simulated model. And the thicknesses of MoS_2 sheet and incident laser wavelength were 6 and 980 nm, respectively. **Figure 10a**, **b** shows the cross-section of the simulated electric field distribution of Au NPs decorated MoS_2. Benefiting from the LSPR effect excited by the Au NPs, when the diameter matched to the incident wavelengths, the intensities of electric field at interfaces of air/Au/MoS_2, up to ~3.96 × 10^5 V/m, are obviously higher than other districts. In comparison, interfaces of air/MoS_2 show a poor intensity of electric field, only about 6.72 × 10^4 V/m. This tendency can be also observed in the recent researches of Au NPs guided MoS_2 sheets for photo-detection [30]. We further experimentally proved the absorption by using UV-visible-NIR spectroscopy analysis. **Figure 10c** shows the absorption spectrum of bare MoS_2 sheet Au NPs decorated MoS_2. The normalized absorptance plots indicate that the Au NPs/MoS_2 is obviously enhanced than that of bare MoS_2 ranging from 700 to 1600 nm.

The above results and discussion clearly unveil the introduction of Au NPs plays a key role in enhancing the light matter interactions of MoS_2 with infrared wavelengths. The significantly improved sensitivity of the fabricated photodetector could be attributed to the LSPR effect, shown in **Figure 10d**, induced by the periodically aligned Au NPs, resulting in obvious improvement of local electric field. When the incident infrared wavelengths highly confined by the deposited Au NPs, the local electric field at the interface of Au/MoS_2 is greatly improved by the surface plasmon waves. Firstly, the Au surface plasmons effectively excite a

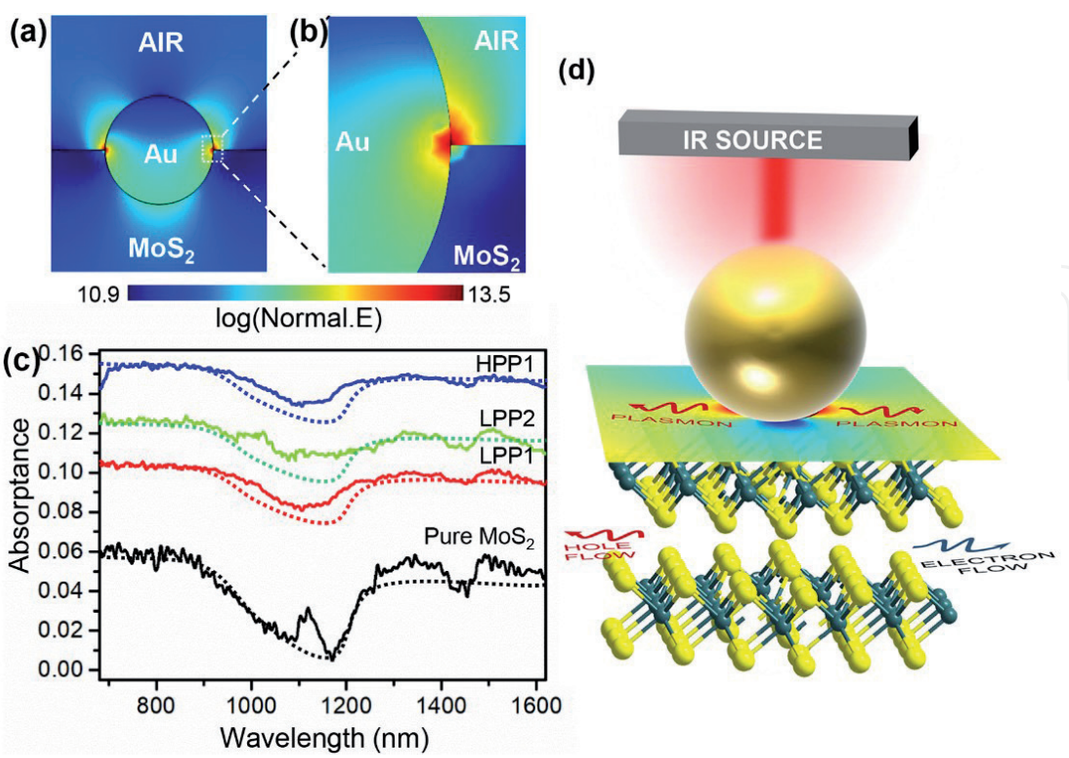

Figure 10.
Cross-section of the simulated electric field distribution for (a) Au NPs/MoS_2 sensing layer and (b) air/Au/MoS_2 interfaces. (c) Absorptance plots of bare MoS_2 sheet and Au NPs decorated MoS_2 using sputtering method. The solid and dashed lines correspond to the experimental and fitted results, respectively. (d) Schematic representation for the operational mechanism of the fabricated Au NPs/MoS_2 device [23].

coupling effect at the interface of Au/MoS_2 for absorbing photons, yielding a much more photo-induced carriers to improve the photo sensing [30, 31]. Moreover, the additional local electric field generated by the LSPR effect of Au NPs accelerates the photogenerated carriers to separate for producing photocurrent [32, 33]. This facile method, tuning Au NPs by sputtering method to excite LSPR effect for fabricating the unique device structure, is expected to be practical applications in other 2D materials such as WS_2 and $MoSe_2$ [34–36], thus offers a new route on a variety of high-performance optoelectronic devices.

4. Conclusion

High performance photodetectors are very important in a lot of applications. We have successfully developed two simple methods to prepare plasmon-enhanced photodetectors. (i) Au nanoparticles (Au NPs) solution were directly spun coated onto the WS_2-based photodetectors. The performance has been enhanced by the LSPR of Au NPs, and reached an excellent high responsivity of 1050 A/W at the wavelength of 590 nm. (ii) Au NPs were deposited on MoS_2 by magnetron sputtering. The spectral response of pure MoS_2 was located in visible light and which was extended to near-infrared region (700–1600 nm) by Au NPs. Further, the responsivity reaching up to 64 mA/W when the incident light is 980 nm. These photodetectors achieved excellent responsivity and response speed. The results not only promote the development of high-performance photodetectors, but also provide a simplified method for the fabrication of other hybrid structure devices.

Acknowledgements

The project was supported by grants from the National Basic Research Program of China (No. 2015CB351905), the National Key Research and Development Program of China (No. 2016YFA 0302300, No. 2016YFA0200400), the National Natural Science Foundation of China (No. 61306105).

Conflict of interest

The authors declare no conflict of interest.

Author details

Yu Liu[1†], Junxiong Guo[2*†], Jianfeng Jiang[3], Wenjie Chen[1], Linyuan Zhao[1], Weijun Chen[1], Renrong Liang[1*] and Jun Xu[1]

1 Institute of Microelectronics, Tsinghua National Laboratory for Information Science and Technology (TNList), Tsinghua University, Beijing, China

2 State Key Laboratory of Electronic Thin Films and Integrated Devices, School of Electronic Science and Engineering (National Exemplary School of Microelectronics), University of Electronic Science and Technology of China, Chengdu, China

3 School of Microelectronics, Shandong University, Jinan, China

*Address all correspondence to: guojunxiong25@163.com and liangrr@mail.tsinghua.edu.cn

† These authors contributed equally to this work.

References

[1] Sun Z, Chang H. Graphene and graphene-like two-dimensional materials in photodetection: Mechanisms and methodology. ACS Nano. 2014;**8**:4133-4156. DOI: 10.1021/nn500508c

[2] Chen H, Liu H, Zhang Z, et al. Nanostructured photodetectors: From ultraviolet to terahertz. Advanced Materials. 2016;**28**:403-433. DOI: 10.1002/adma.201503534

[3] Castro Neto AH, Guinea F, Peres NMR, et al. The electronic properties of graphene. Reviews of Modern Physics. 2009;**81**:109-162. DOI: 10.1103/RevModPhys.81.109

[4] Geim AK, Novoselov KS. The rise of graphene. Nature Materials. 2007;**6**:183-191. DOI: 10.1038/nmat1849

[5] Stankovich S, Dikin DA, Dommett GHB, et al. Graphene-based composite materials. Nature. 2006;**442**:282-286. DOI: 10.1038/nature04969

[6] Stankovich S, Dikin DA, Piner RD, et al. Synthesis of graphene-based nanosheets via chemical reduction of exfoliated graphite oxide. Carbon. 2007;**45**:1558-1565. DOI: 10.1016/j.carbon.2007.02.034

[7] Zhu Y, Murali S, Cai W, et al. Graphene and graphene oxide: Synthesis, properties, and applications. Advanced Materials. 2010;**22**:3906-3924. DOI: 10.1002/adma.201001068

[8] Liu L, Kumar SB, Ouyang Y, et al. Performance limits of monolayer transition metal dichalcogenide transistors. IEEE Transactions on Electron Devices. 2011;**58**:3042-3047. DOI: 10.1109/ted.2011.2159221

[9] Huo N, Yang S, Wei Z, et al. Photoresponsive and gas sensing field-effect transistors based on multilayer WS_2 nanoflakes. Scientific Reports. 2014;**4**:5209. DOI: 10.1038/srep05209

[10] Furchi M, Urich A, Pospischil A, et al. Microcavity-integrated graphene photodetector. Nano Letters. 2012;**12**:2773-2777. DOI: 10.1021/nl204512x

[11] Sun Z, Liu Z, Li J, et al. Infrared photodetectors based on CVD-grown graphene and pbs quantum dots with ultrahigh responsivity. Advanced Materials. 2012;**24**:5878-5883. DOI: 10.1002/adma.201202220

[12] Liu C-H, Chang Y-C, Norris TB, et al. Graphene photodetectors with ultra-broadband and high responsivity at room temperature. Nature Nanotechnology. 2014;**9**:273-278. DOI: 10.1038/nnano.2014.31

[13] Xu H, Wu J, Feng Q, et al. High responsivity and gate tunable graphene-MoS_2 hybrid phototransistor. Small. 2014;**10**:2300-2306. DOI: 10.1002/smll.201303670

[14] Lee Y, Kwon J, Hwang E, et al. High-performance perovskite-graphene hybrid photodetector. Advanced Materials. 2015;**27**:41-46. DOI: 10.1002/adma.201402271

[15] Su Y, Guo Z, Huang W, et al. Ultra-sensitive graphene photodetector with plasmonic structure. Applied Physics Letters. 2016;**109**:173107. DOI: 10.1063/1.4966597

[16] Liu Y, Huang W, Gong T, et al. Ultra-sensitive near-infrared graphene photodetectors with nanopillar antennas. Nanoscale. 2017;**9**:17459-17464. DOI: 10.1039/c7nr06009b

[17] Liu Y, Gong T, Zheng Y, et al. Ultra-sensitive and plasmon-tunable graphene

photodetectors for micro-spectrometry. Nanoscale. 2018;**10**:20013-20019. DOI: 10.1039/c8nr04996c

[18] Zhao B, Zhao JM, Zhang ZM. Enhancement of near-infrared absorption in graphene with metal gratings. Applied Physics Letters. 2014;**105**:031905. DOI: 10.1063/1.4890624

[19] Fang J, Wang D, DeVault CT, et al. Enhanced graphene photodetector with fractal metasurface. Nano Letters. 2017;**17**:57-62. DOI: 10.1021/acs.nanolett.6b03202

[20] Jiang N, Zhuo X, Wang J. Active plasmonics: Principles, structures, and applications. Chemical Reviews. 2018;**118**:3054-3099. DOI: 10.1021/acs.chemrev.7b00252

[21] Freitag M, Low T, Zhu W, et al. Photocurrent in graphene harnessed by tunable intrinsic plasmons. Nature Communications. 2013;**4**:1951. DOI: 10.1038/ncomms2951

[22] Liu Y, Huang W, Chen W, et al. Plasmon resonance enhanced WS_2 photodetector with ultra-high sensitivity and stability. Applied Surface Science. 2019;**481**:1127-1132. DOI: 10.1016/j.apsusc.2019.03.179

[23] Guo JX, Li SD, He ZB, et al. Near-infrared photodetector based on few-layer MoS_2 with sensitivity enhanced by localized surface plasmon resonance. Applied Surface Science. 2019;**483**: 1037-1043. DOI: 10.1016/j.apsusc.2019.04.044

[24] Komsa H-P, Krasheninnikov AV. Electronic structures and optical properties of realistic transition metal dichalcogenide heterostructures from first principles. Physical Review B. 2013;**88**:085318. DOI: 10.1103/PhysRevB.88.085318

[25] Fedutik Y, Temnov VV, Schoeps O, et al. Exciton-plasmon-photon conversion in plasmonic nanostructures. Physical Review Letters. 2007;**99**:136802. DOI: 10.1103/PhysRevLett.99.136802

[26] Baker MA, Gilmore R, Lenardi C, et al. XPS investigation of preferential sputtering of S from MoS_2 and determination of MoS_x stoichiometry from Mo and S peak positions. Applied Surface Science. 1999;**150**:255-262. DOI: 10.1016/s0169-4332(99)00253-6

[27] Ambrosi A, Sofer Z, Pumera M. Lithium intercalation compound dramatically influences the electrochemical properties of exfoliated MoS_2. Small. 2015;**11**:605-612. DOI: 10.1002/smll.201400401

[28] Huang X, Li S, Huang Y, et al. Synthesis of hexagonal close-packed gold nanostructures. Nature Communications. 2011;**2**:292. DOI: 10.1038/ncomms1291

[29] Lee C, Yan H, Brus LE, et al. Anomalous lattice vibrations of single- and few-layer MoS_2. ACS Nano. 2010;**4**:2695-2700. DOI: 10.1021/nn1003937

[30] Wu ZQ, Yang JL, Manjunath NK, et al. Gap-mode surface-plasmon-enhanced photoluminescence and photoresponse of MoS_2. Advanced Materials. 2018;**30**:1706527. DOI: 10.1002/adma.201706527

[31] Miao JS, Hu WD, Jing YL, et al. Surface plasmon-enhanced photodetection in few layer MoS_2 phototransistors with Au nanostructure arrays. Small. 2015;**11**:2392-2398. DOI: 10.1002/smll.201403422

[32] Sun YH, Liu K, Hong XP, et al. Probing local strain at MX_2-metal boundaries with surface plasmon-enhanced Raman scattering. Nano Letters. 2014;**14**:5329-5334. DOI: 10.1021/nl5023767

[33] Bang S, Duong NT, Lee J, et al. Augmented quantum yield of a 2D monolayer photodetector by surface plasmon coupling. Nano Letters. 2018;**18**:2316-2323. DOI: 10.1021/acs.nanolett.7b05060

[34] Zhao W, Wang S, Liu B, et al. Exciton-plasmon coupling and electromagnetically induced transparency in monolayer semiconductors hybridized with Ag nanoparticles. Advanced Materials. 2016;**28**:2709-2715. DOI: 10.1002/adma.201504478

[35] Abid I, Chen W, Yuan J, et al. Temperature-dependent plasmon exciton interactions in hybrid Au/$MoSe_2$ nanostructures. ACS Photonics. 2017;**4**:1653-1660. DOI: 10.1021/acsphotonics.6b00957

[36] Abid I, Bohloul A, Najmaei S, et al. Resonant surface plasmon-exciton interaction in hybrid MoSe2@Au nanostructures. Nanoscale. 2016;**8**:8151-8159. DOI: 10.1039/c6nr00829a